

Electronic Modulation and Mechanistic Study of Ru-Decorated Porous Cu-Rich Cuprous Oxide for Robust Alkaline Hydrogen Oxidation and Evolution Reactions

Yi Liu,^[a] Lianrui Cheng,^[a] Yi Huang,^[a] Yuting Yang,^[a] Xianfa Rao,^{*,[b]} Shuqing Zhou,^[a] Tayirjan Taylor Isimjan,^{*,[c]} and Xiulin Yang^{*,[a]}

Rational design of high-efficiency and viable electrocatalysts is essential in overcoming the bottleneck of sluggish alkaline hydrogen oxidation/evolution reaction (HOR/HER) kinetics. In this study, a metal-organic framework-derived strategy for constructing a Pt-free catalyst with Ru clusters anchored on porous Cu–Cu₂O@C is proposed. The designed Ru/Cu–Cu₂O@C exhibits superior HOR performance, with a mass activity of 2.7 mA μg_{Ru}⁻¹ at 50 mV, which is about 24 times higher than that of state-of-the-art Pt/C (0.11 mA μg_{Pt}⁻¹). Significantly, Ru/Cu–Cu₂O@C also displays impressive HER performance by

generating 26 mV at 10 mA cm⁻², which exceeds the majority of documented Ru-based electrocatalysts. Systematic characterization and density functional theory (DFT) calculations reveal that efficient electron transfer between Ru and Cu species results in an attenuated hydrogen binding energy (HBE) of Ru and an enhanced hydroxy binding energy (OHBE) of Cu₂O, together with an optimized H₂O adsorption energy with Cu₂O as the H₂O*-capturing site, which jointly facilitates HOR and HER kinetics.

Introduction

The ongoing depletion of fossil fuels and consequent environmental issues are urging the development of sustainable energy conversion and storage systems. Hydrogen has been advocated as the most attractive alternative to replace fossil fuels owing to its cleanliness, high energy density and zero-carbon emissions. HOR and HER are two elementary electrode reactions of fuel cells and electrolyzer, respectively, that are key to a prosperous hydrogen economy.^[1] Fuel cell is an economically promising energy conversion technology that can directly convert chemical energy into electric energy.^[2] Among them, anion-exchange membrane fuel cells (AEMFCs) have attracted increasing attention due to their cost competitiveness and unique advantages of operating in a less-corrosive alkaline environment compared to proton-exchange membrane fuel cells (PEMFCs).^[3] Unfortunately, sluggish HOR kinetics hinder the development of AEMFCs.^[4] Up to now, Pt or Pt-related nano-

materials are deemed as the state-of-the-art HOR/HER electrocatalysts regardless they suffer from scarcity, high cost, and low stability. But their HOR/HER activity decreases by about two orders of magnitude when transitioning from acidic to alkali environment.^[5] Considering the earth-abundant transition metals are compatible with alkali electrolytes, enormous efforts have been devoted to exploring high-efficiency catalysts to drive alkaline HOR/HER.

Ascertaining the reaction mechanism and descriptor is essential in designing a reasonable electrocatalyst. Previous studies have proposed that H₂ is oxidized to water molecules in alkaline HOR mechanism, explicitly following the Tafel-Volmer or Heyrovsky-Volmer steps. Given that the adsorbed hydrogen (H_{ad}) is a crucial intermediate, HBE has been identified as a dominating descriptor for HOR/HER.^[6] According to Sabatier principle, there is a volcanic relationship between reaction activity and the H_{ad} on metals, an ideal HBE with zero Gibbs free energy change for hydrogen adsorption implies the highest HOR/HER activity.^[7] Thus, the slower kinetics may be mainly attributed to a general enhancement of HBE in alkaline condition.^[8] Undeniably, the OHBE might play a significant role in alkali HOR. For example, Yu and co-workers reported that the higher HOR rate of MoNi₄ determines by the synergistic optimization between HBE and OHBE.^[9] Additionally, the novel BCC-phased PdCu reported by Li and co-workers demonstrates that the synergistic interplay of the binding strength of H_{ad} and OH_{ad} enhances HOR activity.^[8]

Ruthenium (Ru) has HBE properties similar to Pt but at a much lower price, having a tremendous cost advantage, making it the most promising alternative to Pt.^[10] Ru is regarded as a performance enhancer as a small amounts can improve various electrochemical properties of the original material.^[11] For instance, Yang and co-workers demonstrated that NC@WOC

[a] Y. Liu, L. Cheng, Y. Huang, Y. Yang, S. Zhou, Prof. Dr. X. Yang
Guangxi Key Laboratory of Low Carbon Energy Materials
School of Chemistry and Pharmaceutical Sciences
Guangxi Normal University, Guilin, 541004 (P. R. China)
E-mail: xlyang@gxnu.edu.cn

[b] Dr. X. Rao
School of Resources and Environmental Engineering
Jiangxi University of Science and Technology, Ganzhou, 341000 (P. R. China)
E-mail: raioxianfa@126.com

[c] Dr. T. Taylor Isimjan
Saudi Arabia Basic Industries Corporation (SABIC) at King Abdullah
University of Science and Technology (KAUST)
Thuwal, 23955-6900 (Saudi Arabia)
E-mail: isimjant@sabic.com

Supporting information for this article is available on the WWW under
<https://doi.org/10.1002/cssc.202202113>

decorated with Ru clusters exhibits superior exchange-current density for HOR.^[12] Moreover, an excellent metal-support interface produced by the introduction of carbon supports can effectively augment the catalytic activity, which is of great significance for heterogeneous electrocatalysts. Metal-organic frameworks (MOFs) are porous crystal materials composed of multifunctional organic linkers and metal species in a specific combination.^[13] MOFs have the characteristics of adjustable porosity, large specific surface area and remarkable selectivity, which can be applied as precursors to synthesize catalysts with high chemical stability and excellent catalytic performance.^[14] Interestingly, pyrolysis of these MOF precursors in an inert atmosphere can convert organic ligands into porous graphite carbon, and carbon-coated clusters can be obtained in situ.^[15]

Herein, we launched a plan to convert appropriate MOF precursors into highly porous and eminent conductive electrocatalysts with controllable components through annealing benefiting from the modular nature and excellent MOF adjustability. Specifically, starting from Cu-MOF with a porous octahedral structure, Ru clusters were anchored on the Cu–Cu₂O@C matrix and further pyrolyzed under an inert atmosphere. The as-obtained Ru/Cu–Cu₂O@C manifested remarkable performance in alkaline environment. The HOR mass activity (2.7 mA μg_{Ru}⁻¹) is nearly 24-folds higher than that of Pt/C (0.11 mA μg_{Pt}⁻¹). Additionally, it exhibited superior HER with an overpotential as low as 26 mV at 10 mA cm⁻² accompanied by a slight Tafel slope of 28.7 mV dec⁻¹. Experimental results and DFT calculations confirmed that such enhanced HOR/HER performance was derived from effective electron transfer between Ru and Cu species, leading to the attenuated HBE and strengthened OHBE, as well as ideal H₂O adsorption energy.

Results and Discussion

Synthetic strategy and structural analysis

The Ru/Cu–Cu₂O@C was synthesized as illustrated in Figure 1a. The octahedral Cu-BTC was synthesized via coordination reactions between Cu nodes and organic linkers at room temperature using Cu(NO₃)₂·3H₂O as Cu source, trimesic acid (H₃BTC) as the organic ligand and polyvinylpyrrolidone (PVP) as adjuncts. Subsequently, the Ru precursor was adsorbed onto the Cu-BTC porous octahedral to form Ru/Cu-BTC. X-ray diffraction (XRD) analysis of Ru species before and after loading showed no significant changes (see the Supporting Information, Figure S2), indicating that the MOF skeleton was not damaged during the Ru loading process. Finally, Ru/Cu-BTC evolved into the Ru/Cu–Cu₂O@C through the thermal treatment under N₂ atmosphere at 600 °C (denoted as Ru/Cu–Cu₂O@C-600). During the carbonization, Cu species were transformed into Cu–Cu₂O@C heterojunction structure with the co-presence of Cu and Cu₂O, which are partially protected by graphene layers. As evidenced by thermogravimetric (TG) analysis in Figure S3, the pyrolysis temperature of Ru/Cu-BTC was fixed at 600 °C. The XRD peaks were ascribed to Ru/Cu–Cu₂O@C composites (Figure 1b), demonstrating formation of the target catalyst. Expressly, three characteristic peaks for Cu (JCPDS: 04-0836) at 43.3, 50.4, and 71.1° corresponded to (111), (200), (220) lattice planes respectively, and the sharp diffraction peaks indicated its high crystallinity.^[16] The additional XRD peaks could be ascribed to the Cu₂O species (JCPDS: 78-2076). Notably, no peaks were attributed to Ru, revealing relatively low crystallinity and small particle sizes. For comparison, Figure S4a–b confirmed the

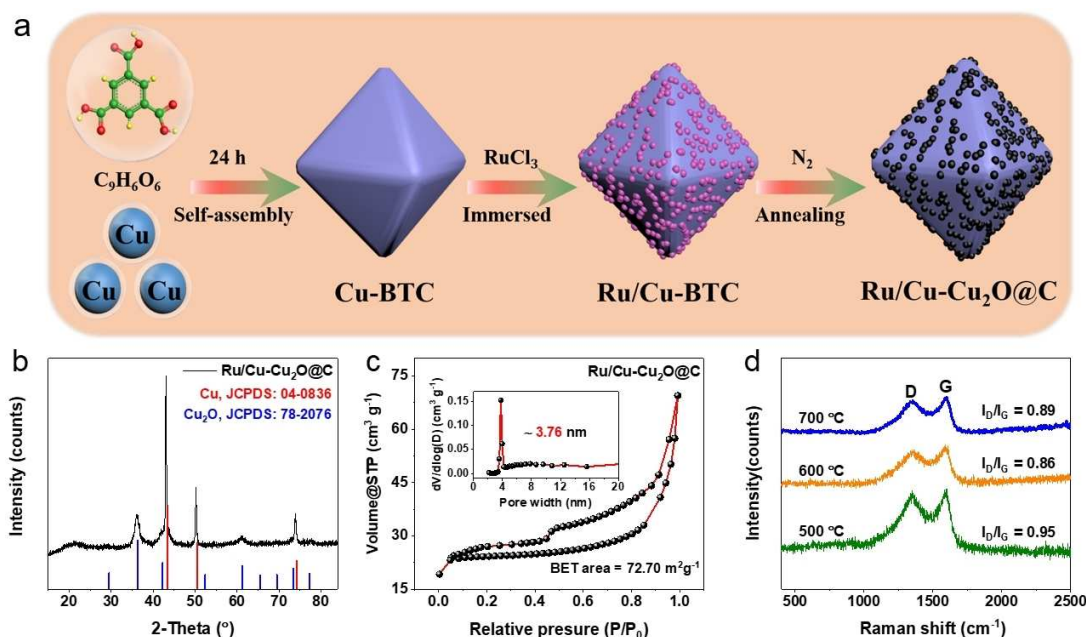


Figure 1. (a) Schematic illustration of the preparation of Ru/Cu–Cu₂O@C. (b) XRD pattern of Ru/Cu–Cu₂O@C. (c) N₂ adsorption-desorption isotherms with corresponding pore size distribution (inset) of Ru/Cu–Cu₂O@C. (d) Raman spectra of Ru/Cu–Cu₂O@C at different temperatures.

formation of Ru/Cu@C and Ru/Cu₂O@C without crystalline impurities.

The N₂ adsorption-desorption isotherm (Figure 1c) exhibited an obvious hysteresis loop with typical IV isotherm, confirming mesoporous existence.^[17] Specifically, such a unique porous structure contributed to a high Brunauer–Emmett–Teller surface area of 72.7 m² g⁻¹ with an adsorption average pore diameter of 3.76 nm, further implying the presence of mesopores in Ru/Cu–Cu₂O@C.^[18] The broad D (1346 cm⁻¹) and G (1589 cm⁻¹) bands of carbon provided in Raman spectroscopy corresponded to the defect/disorder density and graphitization of carbon.^[19] Ru/Cu–Cu₂O@C-600 gave the lowest I_D/I_G value of 0.86, compared to Ru/Cu–Cu₂O@C-500 (0.95) and Ru/Cu–Cu₂O@C-700 (0.89), evidencing more sp²-hybridized carbon existed in Ru/Cu–Cu₂O@C-600, which was favorable for accelerating charge transfer (Figure 1d).^[20]

Scanning electron microscopy (SEM) and transmission electron microscopy (TEM) were applied to ascertain the morphology of Ru/Cu–Cu₂O@C. During thermal decomposition, Cu-BTC was transformed into Ru/Cu–Cu₂O@C with good crystallinity and high monodispersity due to the Ostwald ripening effect.^[21] Ru/Cu–Cu₂O@C retained its initial octahedral shape with a rougher surface than Cu-BTC precursor (Figure 2a,b). Interestingly, such porous octahedral structure obtained by pyrolysis was beneficial to exposing more active sites and facilitating the rapid release of gas molecules, which

effectively accelerated the contact of reactants with active sites, thereby enhancing the HOR/HER catalytic performance.^[22]

Further TEM observations (Figure 2c,d) revealed that the highly uniform and discrete Ru clusters with an average size of about 1.53 nm were well distributed on Cu–Cu₂O@C support.^[23] High-resolution transmission electron microscopy (TEM; Figure 2e) clearly showed the presence of Ru, Cu, and Cu₂O crystal phases. The well-defined lattice fringes, with inter-planar distances of approximately 0.238 and 0.214 nm, were identified as the (100) and (002) planes of Ru. The lattice distance of 0.246 and 0.213 nm was found to correspond to the (111) and (200) planes of Cu₂O, and the lattice distance of 0.208 nm was attributed to the (111) plane of metallic Cu. HAADF-STEM image and corresponding elemental mappings (Figure 2f) of Ru/Cu–Cu₂O@C affirmed the homogeneous distribution of Cu, Ru, C, and O elements throughout the entire architecture.^[24]

X-ray photoelectron spectroscopy analysis

Further insights into the unique electron structure after Ru doping were obtained from X-ray photoelectron spectroscopy (XPS). The fundamental elements of Cu, Ru, O, and C were detected in the survey spectrum of Ru/Cu–Cu₂O@C (Figure 3a), further affirming its elemental composition. In the fitting process of XPS, we strictly followed the elementary rules of

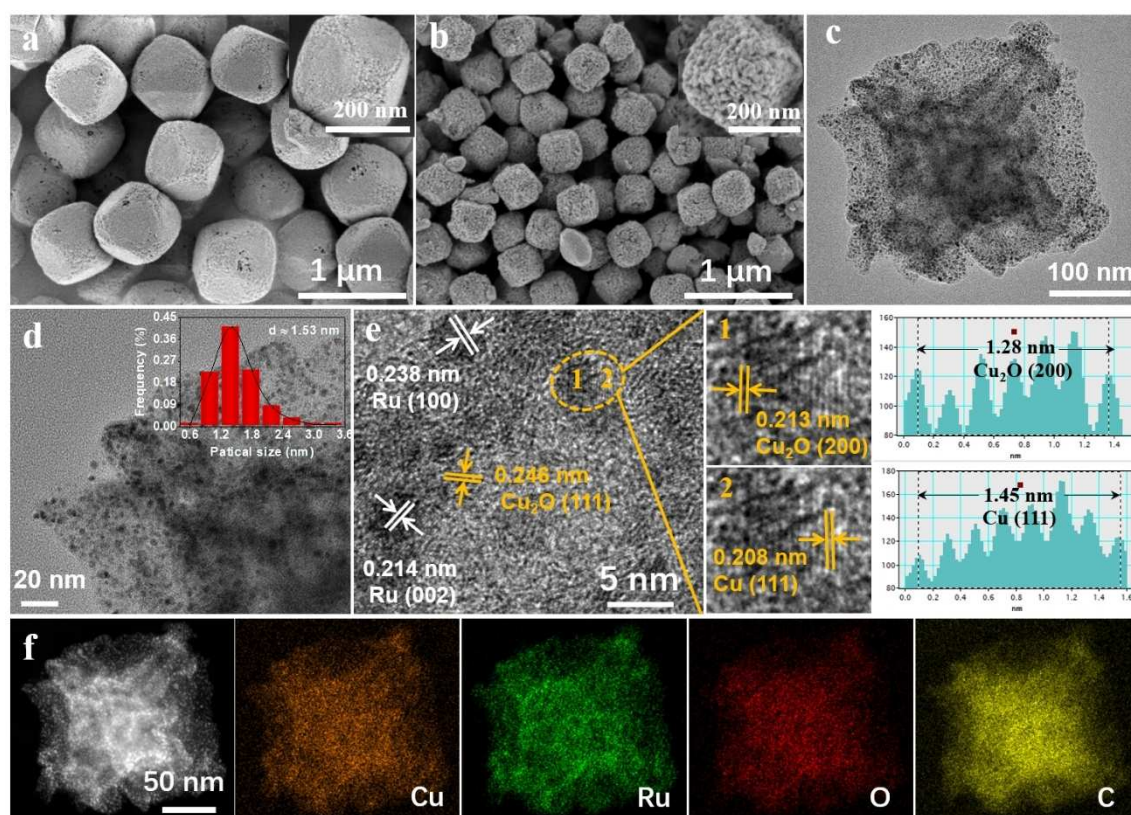


Figure 2. (a,b) SEM images of (a) Cu-BTC and (b) Ru/Cu–Cu₂O@C. (c,d) TEM images of Ru/Cu–Cu₂O@C. (e) High-resolution TEM and the corresponding lattice spacing profiles of the dotted line regions of Ru/Cu–Cu₂O@C. (f) HAADF-STEM image and corresponding elemental mappings of Ru/Cu–Cu₂O@C.

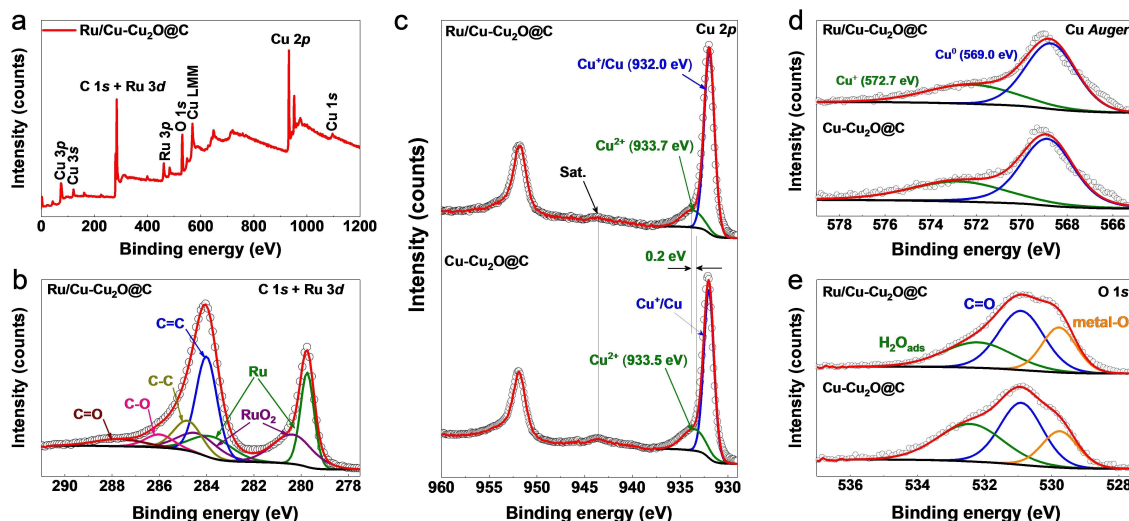


Figure 3. (a) XPS survey spectrum of Ru/Cu–Cu₂O@C. High-resolution XPS spectra of (b) C 1s + Ru 3d, (c) Cu 2p, (d) Cu Auger, (e) O 1s.

peak fitting. The XPS spectra of C=C (284.0 eV), C–C (284.8 eV) and C–O (286.0 eV) in C 1s + Ru 3d regions were deconvoluted as calibration criteria (Figure 3b). Meanwhile, the Ru 3d_{5/2} peaks were performed by two groups of peaks at the BE of 279.6, 283.6 eV and 280.2, 284.2 eV, corresponding to metallic Ru and Ru oxide, respectively.^[25] Note that the occurrence of Ru oxide was probably owing to the partial surface oxidation of the adsorbed oxygen when the sample was exposed to air.^[26] Two components accomplished the fittings of Cu 2p_{3/2} core level with BE of 933.7 and 932.0 eV.

The XPS spectrum peak at 932.0 eV was assigned to Cu⁺ or Cu⁰, while the peak at 933.7 eV was typically attributed to Cu²⁺ species (Figure 3c). Considering the high-resolution XPS spectra of Cu 2p_{3/2} cannot distinguish between Cu⁰ and Cu⁺, X-ray induced Auger spectrum was further applied to confirm the existence of Cu⁺ at 572.7 eV (Figure 3d). Above results suggested that numerous Cu²⁺ was successfully transformed into Cu⁺ and Cu⁰, which were in good agreement with XRD results.^[27] Notably, the typical Cu–O in Ru/Cu–Cu₂O@C illustrated a positive shift by 0.2 eV compared to Cu–Cu₂O@C. This phenomenon indicated that the doping of Ru decreased the outer electron cloud density of Cu species, weakening the shielding effect.^[28] XPS analysis confirmed the electronic interaction between Ru and Cu–Cu₂O@C, proving that Ru could modulate the electronic structure of Cu species, thereby quickening the kinetics of HOR/HER process. Furthermore, the peak-fitting analysis of O 1s spectra (Figure 3e) displayed that three chemical states consisted of Ru/Cu–Cu₂O@C. The peak at 529.7 eV was occupied by metal oxide such as Cu₂O, the other peaks located at 530.8 and 532.4 eV corresponding to C=O and adsorbed H₂O, respectively.^[21]

Electrochemical HOR performance

We systematically investigated their electrochemical performance based on the successful synthesis and comprehensive characterization of electrocatalysts. Firstly, since the Ru content and annealing temperature significantly affected the HOR catalytic activity of Ru/Cu–Cu₂O@C, a series of optimization experiments were carried out (Figure S5). We fixed the annealing temperature at 600 °C based on the TGA results. And the optimal loading of Ru in Ru/Cu–Cu₂O@C was 4.76 wt%, confirmed by inductively coupled plasma atomic emission spectrometry (ICP-AES; Table S1), exhibiting the best HOR performance. Afterwards, we evaluated the HOR performance using a rotating disk electrode (RDE) voltammetry in a standard three-electrode system. Cyclic voltammetry (CV) curves of these samples were tested at a scan rate of 50 mV s^{−1} in N₂-saturated 0.1 M KOH electrolyte (Figure S6) to understand hydrogen adsorption-desorption behaviors. Previous studies demonstrated that the hydrogen underpotential deposition (H_{upd}) peaks were related directly to HBE, and the HBE became stronger with the increasing hydrogen desorption peak potential. Nevertheless, stronger HBE was the main reason for slower HOR kinetics.^[29] The Ru/Cu–Cu₂O@C catalyst showed a H_{upd} peak potential for hydrogen adsorption-desorption at around 0.20 V vs. RHE, indicating weaker binding of hydrogen on the Ru metal sites. This peak was negatively shifted compared to Pt/C (0.32 V vs. RHE), which suggested that the HBE of Ru/Cu–Cu₂O@C was weaker and thus it accelerated the Volmer step in the alkaline HOR. Inversely, Cu–Cu₂O@C and benchmark Ru/C exhibited unremarkable hydrogen adsorption-desorption behavior, revealing that the strong coordination interaction between Ru species and Cu–Cu₂O@C could weaken HBE.

Figure 4a depicted the HOR polarization curves of as-prepared samples, apparently, Ru/Cu–Cu₂O@C possessed the highest anodic current density, and the initial potential as low as 0 V vs. RHE, highlighting its extraordinary capacity for alkaline

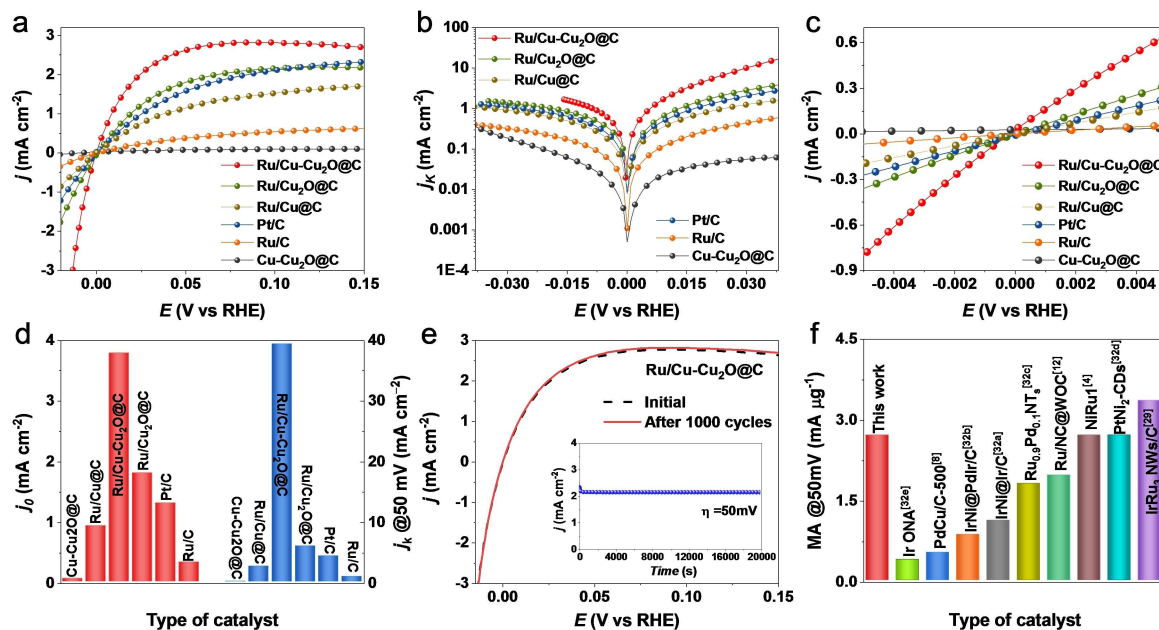


Figure 4. (a) HOR polarization curves in H_2 -saturated 0.1 M KOH at a scan rate of 10 mV s^{-1} and a rotating speed of 1600 rpm. (b) Tafel plots of j_k . (c) Linear fitting curves in micro-polarization region (-5 to 5 mV). (d) j_0 at 50 mV and j_0 of different studied catalysts. (e) Accelerated durability test and chronoamperometric response of Ru/Cu–Cu₂O@C. (f) Mass activity (MA) at 50 mV and other recently reported alkaline HOR electrocatalysts.^[4,8,12,29,32]

HOR.^[30] Furthermore, we performed comparative experiments in N_2 -saturated 0.1 M KOH electrolyte (Figure S7), and Ru/Cu–Cu₂O@C exhibited negligible anodic current across the entire potential range, implying the anodic current was indeed owing to H_2 oxidation. In Figure S8, the HOR polarization curves of various catalysts at different rotation speeds ranging from 400 to 2500 rpm were shown. The plateau current densities of Ru/Cu–Cu₂O@C were found to increase as the rotation speed increased, which was attributed to improved mass transport at higher rotation rates.^[4] This was further verified through a Koutecky-Levich plot that yielded a value of $12.09 \text{ cm}^2 \text{ mA}^{-1} \text{ rpm}^{1/2}$, indicating that the process was primarily controlled by H_2 mass transport.^[31] The HOR activity of Ru/Cu–Cu₂O@C and referenced samples were quantitatively assessed by kinetic current density (j_k) that non-linearly fitted the HOR polarization curves. In Figure 4b, Ru/Cu–Cu₂O@C behaved as an outstanding anode material in H_2 oxidation region with the highest j_k value at random fixed potentials.

Exchange current density (j_0) was determined by linearly fitting of micro-polarization region (-5 – 5 mV) using simplified Butler-Volmer formula (Figure 4c), where the slope was proportional to j_0 . Ru/Cu–Cu₂O@C displayed the highest slope among our studied catalyst, implying the topmost HOR activity. As shown in Figure 4d, the j_0 of Ru/Cu–Cu₂O@C (3.77 mA cm^{-2}) was 3-folds and 12-folds higher than those of Pt/C (1.30 mA cm^{-2}) and Ru/C (0.32 mA cm^{-2}), respectively. Meanwhile, the Ru/Cu–Cu₂O@C catalyst possessed a j_k of 39.29 mA cm^{-2} at 50 mV , outperforming other studied catalysts. Ru/Cu–Cu₂O@C performed a long-term HOR process at a current density of 50 mA cm^{-2} . The two polarization curves almost overlap. The inset presented a stable current density, at

constant potential for 1000 s, implying good stability during HOR process (Figure 4e). As shown in Figure S9, the Ru/Cu–Cu₂O@C-After catalyst retained its original morphology, with only minor structural collapse observed. Additionally, XPS analysis revealed that the Ru/Cu–Cu₂O@C-After catalyst still contained signals for Ru, Cu, Cu⁺, with a notable increase in the Cu²⁺ signal. This is in line with the theoretical results that suggested that this was caused by the prolonged H_2 oxidation process (Figure S10). Ru/Cu–Cu₂O@C displayed a higher mass-activity ($2.7 \text{ mA } \mu\text{g}_{\text{Ru}}^{-1}$) at 50 mV (Figure 4f and Table S3), substantially exceeding most reported HOR catalysts.^[4,8,12,29,32] Moreover, we summarized the HOR performance parameters of studied catalysts (Table S2).

Since Ru interfered with hydrogen desorption/adsorption sites, the hydrogen under-potential deposition region was not suitable for calculating the electrochemical active surface area (ECSA) of the samples. Thus, we adopted CO-stripping voltammetry to calculate the ECSA value.^[33] The ECSA of Ru/Cu–Cu₂O@C was found to be $154.65 \text{ m}^2 \text{ g}^{-1}$ (Figure S11), which is significantly higher than those of commercial Pt/C ($73.2 \text{ m}^2 \text{ g}^{-1}$) and benchmark Ru/C ($10.42 \text{ m}^2 \text{ g}^{-1}$). A higher ECSA was favorable for exposing more catalytic active sites, facilitating sufficient contact between reactants and electrolytes.^[34] When normalized by the ECSA values, the Ru/Cu–Cu₂O@C demonstrated a much higher $j_{0,s}$ of 0.17 mA cm^{-2} , outperforming that of Pt/C, indicating strong intrinsic HOR activity of Ru/Cu–Cu₂O@C (Table S2).

Electrochemical HER performance

HER was the reverse reaction of HOR. Encouraged by the outstanding performance of Ru/Cu–Cu₂O@C for alkaline HOR, we further recorded its HER performance. Firstly, the Ru loading and pyrolysis temperatures were optimized to find the ideal synthesis conditions (Figure S12). The HER activities were measured by linear sweep voltammetry (LSV) in H₂-saturated 1.0 M KOH electrolyte. Among them, the high-purity H₂-saturated electrolyte was adopted to restrain the absorption and dissolution of CO₂ and fasten the reversible hydrogen potential.^[35] In alkaline environment, Ru/Cu–Cu₂O@C exhibited much admirable HER activity (26.0 mV) at a current density of 10 mA cm⁻² compared to other investigated samples (Figure 5a). The Tafel diagram of corresponding polarization curves (Figure 5b) provided an in-depth insight into the HER reaction pathway. Ru/Cu–Cu₂O@C presented the smallest Tafel slope of 28.7 mV dec⁻¹, indicating the fastest HER kinetics.^[36] For alkaline HER, the Volmer step occurred first, where H₂O was reduced to H_{ads} and OH⁻. Volmer step to form H_{ads} was kinetically slow, there were two possible paths for the conversion of H₂: Heyrovsky step or Tafel step. As previously known, Tafel slope of Ru/Cu–Cu₂O@C was lower than Pt/C (35.5 mV dec⁻¹), demonstrating Ru/Cu–Cu₂O@C held a more beneficial kinetic process. The result revealed that Ru/Cu–Cu₂O@C followed Volmer-Tafel mechanism.^[37]

We next compared the performance of Ru/Cu–Cu₂O@C with other documented catalysts containing Ru moieties (Figure 5c and Table S4) and found that Ru/Cu–Cu₂O@C possessed considerable HER activity.^[12,38] The interfacial charge transfers kinetics were investigated by electrochemical impedance spectroscopy (Figure 5d). Apparently, Ru/Cu–Cu₂O@C showed the

smallest charge transfer resistance (R_{ct}), implying the most efficient HER kinetics.^[39] To quantitatively detect the intrinsic catalytic activity of the catalysts, we calculated the turnover frequency (TOF) values using ICP results.^[40] As depicted in Figure 5e, Ru/Cu–Cu₂O@C gave the highest TOF values of all samples, indicating that Cu–Cu₂O@C could be an excellent supporting scaffold for Ru clusters to enhance HER activity intrinsically. Additionally, we performed a long-term durability test of Ru/Cu–Cu₂O@C toward HER (Figure 5f). It exhibited remarkable stability with negligible changes in LSV curve before and after 1000 cycles. Meanwhile, Ru/Cu–Cu₂O@C maintained a stable overpotential throughout the test at 10 mA cm⁻², confirming the excellent stability. After the multi-cycle CV testing, the Ru/Cu–Cu₂O@C-After catalyst retained its initial morphology, however, analysis revealed an increase in the Cu²⁺ signal relative to the Cu and Cu⁺ signals (Figures S13 and S14).

Density functional theory calculations

To further bring theoretical insight into the engaging HOR and HER activities of Ru/Cu–Cu₂O@C, DFT calculations were executed on model systems. In DFT calculations, the choice of crystal planes should match those observed in TEM images. Based on structural characterization and crystal facet stability, the (111) lattice plane of Cu and Cu₂O and the (100) lattice plane of Ru were used for simulations. Figure S15 displayed the optimal structure models of Ru/Cu–Cu₂O@C, Cu–Cu₂O@C, Ru/Cu₂O@C and Ru/Cu@C, respectively (for details, see the Supporting Information). The density of states (DOS; Figure 6a) demonstrated that the d-band center of Ru/Cu–Cu₂O@C was more negatively shifted from the Fermi level than those of

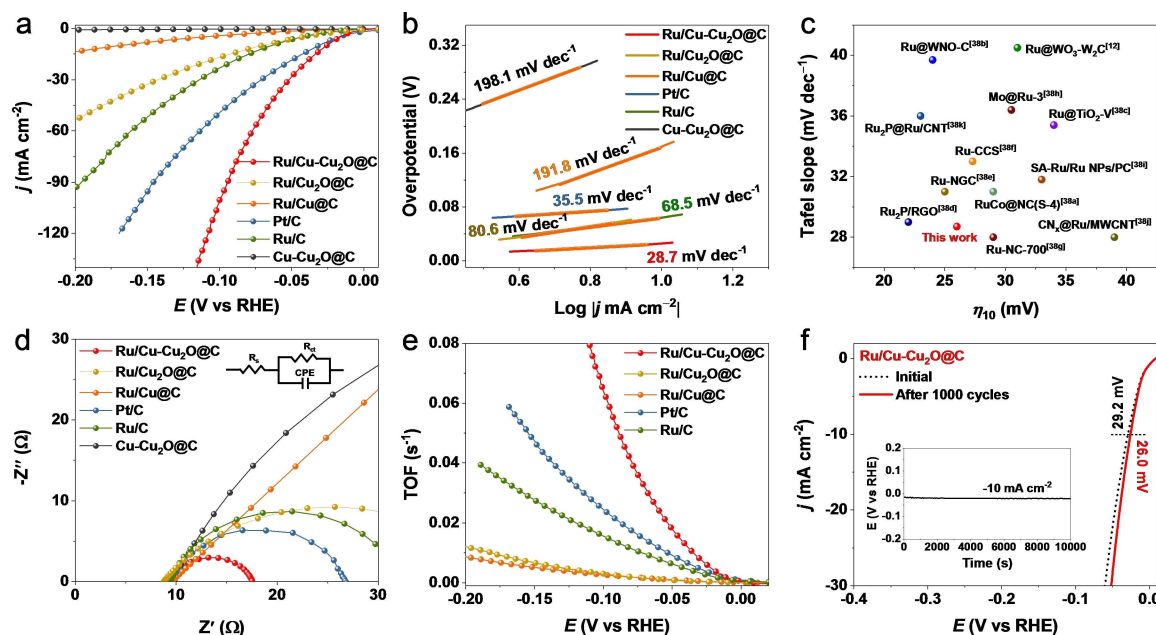


Figure 5. (a) HER polarization curves with a scan speed of 10 mV s⁻¹ at 1600 rpm. (b) Tafel slopes of as-obtained catalysts. (c) Compared the overpotential at 10 mA cm⁻² and Tafel slope of Ru/Cu–Cu₂O@C with recently reported Ru-based catalysts.^[12,38] (d) Nyquist plots. (e) TOF profiles versus potentials of Ru/Cu–Cu₂O@C, Ru/Cu@C, commercial Pt/C, and benchmark Ru/C. (f) Stability of Ru/Cu–Cu₂O@C for 1000 CV cycles in alkaline electrolyte.

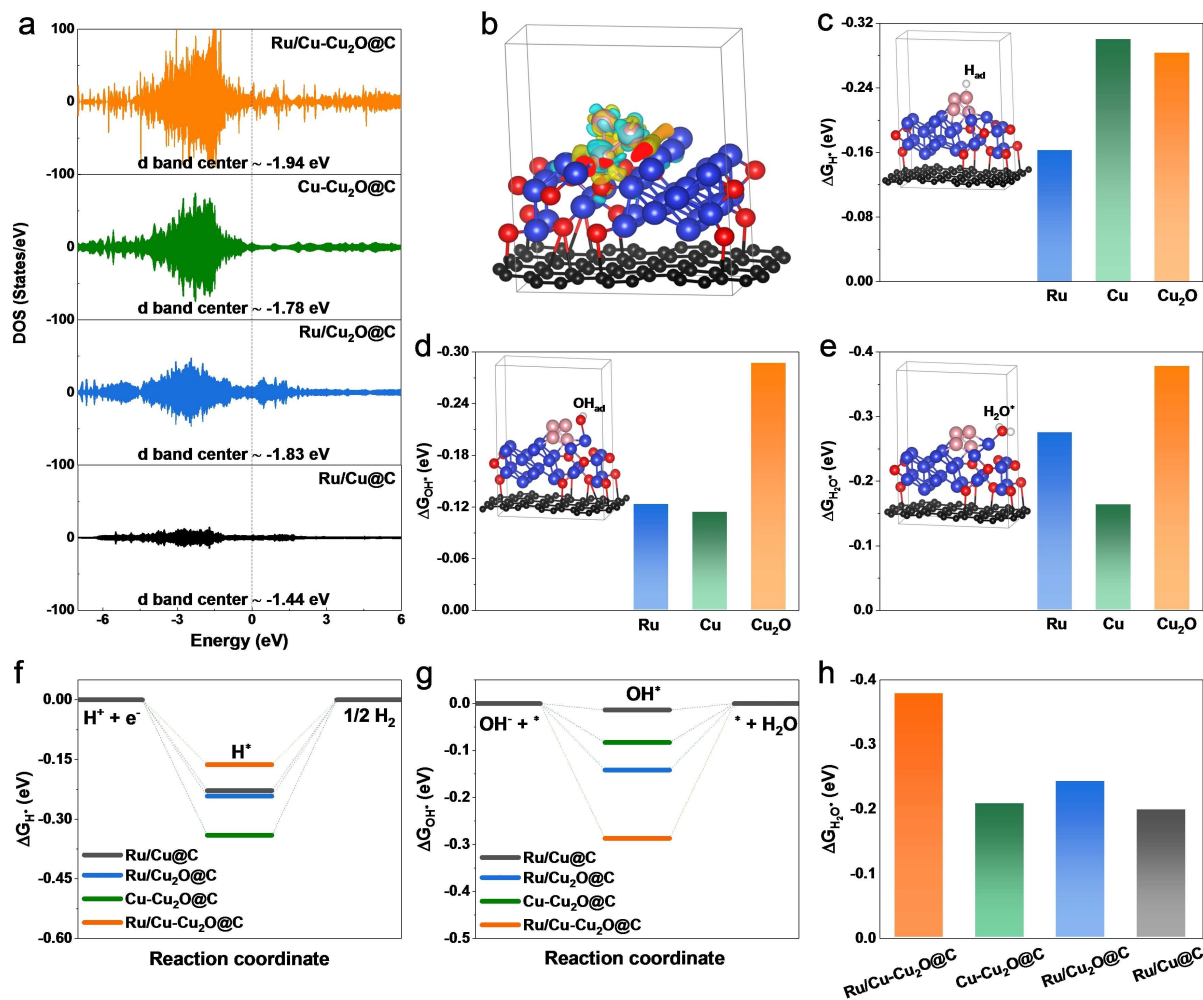


Figure 6. (a) Calculated DOS and corresponding d-band center of Ru/Cu–Cu₂O@C, Ru/Cu@C, Ru/Cu₂O@C and Cu–Cu₂O@C. (b) Charge-density distribution of the Ru/Cu–Cu₂O@C model. (c) Gibbs free energy profiles for hydrogen adsorption (ΔG_{H^*}); the inset shows the optimized hydrogen adsorption configuration on Ru sites. (d) Gibbs free energy profiles for hydroxy adsorption (ΔG_{OH^*}); the inset shows the optimized hydroxy adsorption configuration on Cu₂O sites. (e) Water adsorption energy on Ru, Cu, and Cu₂O in Ru/Cu–Cu₂O@C; the inset shows the optimized water adsorption configuration on Cu₂O sites. (f) ΔG_{H^+} , (g) ΔG_{OH^-} , and (h) water adsorption energies of Ru/Cu–Cu₂O@C, Cu–Cu₂O@C, Ru/Cu₂O@C, and Ru/Cu@C.

Cu–Cu₂O@C (–1.78 eV), Ru/Cu₂O@C (–1.83 eV) and Ru/Cu@C (–1.44 eV). According to the d-band theory by Nørskov and co-workers the lower-lying d-band center can indicate weaker binding interaction between catalysts and adsorbates, which can interpret the reduced H adsorption on Ru/Cu–Cu₂O@C.^[41] Ru/Cu–Cu₂O@C possessed an apparently enhanced DOS around the Fermi level compared to Ru/Cu and Ru/Cu₂O@C, evidencing that it held more carriers for charge transfer and electrical conductivity, which was favorable for catalysis reactions.^[42] Among them, Ru/Cu₂O@C exhibited higher electron density than Ru/Cu@C, which can speculate that the Cu₂O species served as the dominating active sites, and Cu acted as the backup electron reservoir. Notably, d-d coupling between two Cu species prompted the highest electron density of Ru/Cu–Cu₂O@C around the Fermi level, which can promote surface electron transfer, thereby facilitating the performances of HOR/HER.^[43]

Additionally, the differential charge density analysis (Figure 6b) of Ru/Cu–Cu₂O@C revealed an overt charge depletion around Cu and charge accumulation at the interface of Ru, suggestive of a solid electronic interaction between Ru and Cu species.^[44] Both H_{ad} and OH_{ad} were the activity descriptors for HOR catalysis. The cyclic voltammetry behavior (Figure S6) of Ru/Cu–Cu₂O@C revealed that it had the lowest peak potential for hydrogen adsorption–desorption, which indicated the easier desorption and weaker binding to H for Ru/Cu–Cu₂O@C than other catalysts. Given that CO can be specifically adsorbed on many metal surfaces, and OH_{ad} was favorable for removing CO_{ad} intermediates on metal surfaces, we employed CO-stripping voltammetry to characterize the binding of OH⁻ with catalysts. The CO oxidation peak potential of Ru/Cu–Cu₂O@C was located at 0.702 V, while that of Ru/Cu@C exhibited a peak in 0.686 V (Figure S11). Compared with previous two catalysts, Ru/Cu₂O@C displayed a lower CO oxidation peak at 0.664. Apparently, the CO oxidation peak of Ru/Cu₂O@C was negatively shifted relative

to the other two catalysts, demonstrating that Cu₂O moieties with oxophilicity can provide stronger OH⁻ adsorption sites. Based on above results, we investigated various possible sites on Ru, Cu, and Cu₂O position in Ru/Cu–Cu₂O@C to calculate their adsorption free energies of H* (ΔG_{H^*}) and adsorption free energies of OH* (ΔG_{OH^*} ; Figures S16 and S17). Ru/Cu–Cu₂O@C had ideal adsorption sites of H_{ad} and OH_{ad}. As revealed in Figure 6c, Ru in Ru/Cu–Cu₂O@C exhibited the optimal ΔG_{H^*} of –0.16 eV compared to Cu (–0.30 eV) and Cu₂O (–0.28 eV), which was much close to the theoretical ideal value ($\Delta G_{H^*} = 0$ eV).^[30] It manifested that the much-weakened HBE on Ru owing to the synergistic electronic effect of Ru and Cu species, which effectively facilitates the Volmer step for alkali HOR, resulting in the enhanced HOR.^[44] Likewise, Cu₂O in Ru/Cu–Cu₂O@C presented the optimal ΔG_{OH^*} of –0.27 eV, implying more apparent adsorption behavior compared with Ru (–0.12 eV) and Cu (–0.11 eV), which confirmed that surface OH* combines with the highly oxophilic Cu₂O (Figure 6d). For the HER mechanism (Figure 6e and Figure S18), Cu₂O in Ru/Cu–Cu₂O@C exhibited the lowest adsorption free energies of H₂O* ($\Delta G_{H_2O^*}$; –0.38 eV) than Ru (–0.27 eV) and Cu (–0.16 eV), suggesting that H₂O adsorption on Cu₂O surface can easily form Cu₂O–H₂O state than those of Ru and Cu, which resulted in the breaking of HO–H bonds in H₂O, forming H_{ad} on adjacent Ru sites and combined to form H₂.^[45]

Furthermore, we simulated the adsorption behavior of the surfaces with reaction intermediates on Ru/Cu–Cu₂O@C, Cu–Cu₂O@C, Ru/Cu₂O@C and Ru/Cu@C catalysts. Since the adsorption of H* was a critical descriptor for the reaction, a thermally neutral value was required to promote the adsorption-desorption of H*. The calculated ΔG_{H^*} and the optimized configuration are shown in Figure 6f and Figure S19. Compared to the other three catalysts, Ru/Cu–Cu₂O@C had the lowest ΔG_{H^*} , which greatly facilitated the Volmer step in alkaline HOR/HER, resulting in a higher catalytic performance, which is in agreement with our experimental results.^[46] Additionally, we found that Ru/Cu–Cu₂O@C held the strongest OH* adsorption among the four catalysts. Such an enhanced OH* adsorptive behavior favored the capture of OH* species on the Cu₂O surface, in accord with the CO stripping results (Figure 6g and

Figure S20).^[47] Since the dissociation of water was a primary step that directly determined the HER activity, we also calculated the adsorption free energies of H₂O* for the four catalysts (Figure 6h and Figure S21). The values of adsorption free energies of $\Delta G_{H_2O^*}$ on Ru/Cu–Cu₂O@C, Cu–Cu₂O@C, Ru/Cu₂O@C and Ru/Cu@C were –0.38, –0.21, –0.24 and –0.20 eV, respectively. Therefore, Ru/Cu–Cu₂O@C exhibited the strongest binding of water molecules than other three catalysts, accelerating the Volmer step in alkaline HER process.^[48]

Catalytic mechanism

Based on above analysis, a bifunctional mechanism was proposed for augmenting HOR/HER activity of Ru/Cu–Cu₂O@C in alkaline conditions (Figure 7). In respect of HOR, Ru served as a favorable adsorption site for hydrogen intermediates (H_{ad}), and H₂ molecules first dissociated and adsorbed on the surface of Ru metal to form H_{ad} (denoted as Ru–H_{ad}). Meanwhile, Cu₂O acted as an OH-adsorption site to form OH_{ad} (denoted as Cu₂O–OH_{ad}), and finally two intermediate species (H_{ad} and OH_{ad}) reacted to form H₂O. With regards to the HER, according to the Tafel slope analysis (Figure 5b), Ru/Cu–Cu₂O@C followed the Volmer-Tafel mechanism and the Tafel slope of 28.7 mVdec⁻¹ implied that the Tafel reaction (H_{ad} + H_{ad} → H₂) was the rate-determining step over Ru/Cu–Cu₂O@C. Specifically, the water dissociation was promoted by controlling the Volmer step on the Cu₂O surface to generate OH⁻ and H⁺, so that the Cu₂O surface was made to adsorb OH⁻ and H⁺ was immediately adsorbed on Ru clusters. Finally, two adjacent H_{ad} on Ru sites recombined to form H₂ molecules.

Overall, the surprising HOR/HER performance in alkaline environments may be attributed to the following aspects: 1. Strong electronic interaction between Cu–Cu₂O@C substrates and Ru could decrease interfacial impedance and accelerate HOR/HER kinetics. 2. The hierarchical porous structure facilitated the mass/charge transport by creating complete contact of reactants with active sites. 3. Highly conductive of Cu and carbon layer favored electron transmission. 4. The attenuated HBE and enhanced OHBE synergistically promoted the Volmer

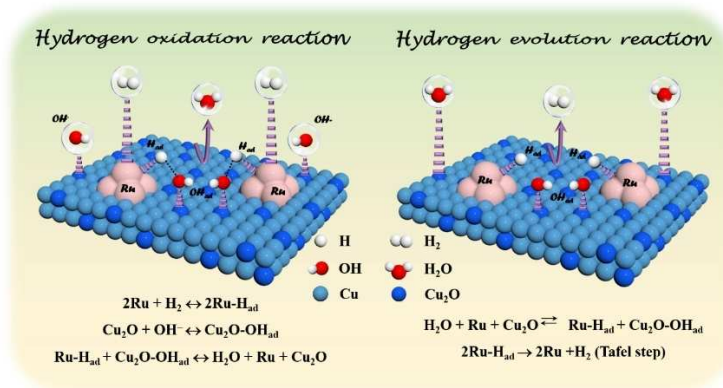


Figure 7. Schematic representation of proposed mechanisms for the alkaline HOR and HER processes over Ru/Cu–Cu₂O@C.

step of HOR, and the optimal H₂O adsorption energy of Cu₂O expedited the Volmer step toward HER.

Conclusion

In summary, we have fabricated an efficient and durable electrocatalyst by using a MOF-derived strategy, where Ru clusters were confined in porous octahedral supports (Ru/Cu–Cu₂O@C). Structurally, this fine-tailoring strategy minimized Ru surface blockage, effectively prevented Ru cluster aggregation, and supplied plenty of reactive centers for electrooxidation of H₂. The optimized Ru/Cu–Cu₂O@C exhibited considerable performance under alkaline conditions with higher mass activity and specific activity toward the HOR process, excellent HER activity with low overpotential at 10 mA cm⁻², and higher stability, outperforming most reported electrocatalysts. Combining experimental results and DFT calculations revealed that the electronic interaction between Ru clusters and Cu–Cu₂O@C support contributed to attenuated HBE and enhanced OHBE, as well as the optimal H₂O adsorption energy, which synergistically accelerated the HOR and HER kinetics. This method would provide a promising approach for the rational synthesis of cost-effective and environmentally friendly bifunctional HOR/HER catalysts.

Experimental Section

Materials

All chemicals and reagents were obtained from pharmaceutical companies that could be used directly without any further purification. Copper nitrate hydrate (Cu(NO₃)₂·3H₂O, AR, 99.5%), trimesic acid (H₃BTC, AR, 99%), ruthenium trichloride (RuCl₃·xH₂O, AR, 99%, ca. 40 wt% Ru), poly(vinylpyrrolidone) [(C₆H₉NO)_n, AR, 99%, PVP], methanol (AR, 99.5%), commercial Pt/C (20 wt% Pt), Nafion solution (5 wt%), deionized water (18.25 MΩ cm⁻¹), potassium hydroxide (KOH, AR, > 90%).

Synthesis of Cu-BTC precursor

Based on previous studies, a Cu-based MOF (Cu-BTC) was synthesized with minor modifications.^[21,49] Briefly, of Cu(NO₃)₂·3H₂O (4 mmol) and PVP (0.8 g) were dissolved in methanol (50 mL) through sonication to afford homogeneous solution A, and H₃BTC (2 mmol) was dissolved in methanol (50 mL) to afford solution B. Solution B was then added to solution A with a dropper and stirred for 30 min until a blue colloidal suspension was formed and aged continuously for 24 h. After the reaction, the resulting blue precipitate was collected by centrifugation with methanol and deionized water, and finally dried in an oven at 60 °C overnight.

Synthesis of Ru/Cu–Cu₂O@C nanocomposites

Typically, as-synthesized Cu-BTC (100 mg) was dispersed in a mixed solution of deionized water/methanol (20 mL, 1:1 v/v) and stirred to form a homogeneous solution. Afterwards, a given amount of 10 mM RuCl₃ solution (1.11, 1.43, or 2.0 mL) was added dropwise to the above suspension and further stirred for 24 h at room temperature. The resulting product was collected by centrifugation with

anhydrous ethanol and deionized water. Subsequently, the brown samples were dried overnight in an oven. Finally, the above as-obtained hybrids were calcined (500 °C, 600 °C, or 700 °C) at a heating rate of 5 °C min⁻¹ for 2 h to afford Ru/Cu–Cu₂O@C nanocomposites. Unless specifically stated, the Ru/Cu–Cu₂O@C was obtained at 600 °C. The Ru content varied from 3.66 wt% to 5.59 wt% and the composites were named as Ru_{3.66}/Cu–Cu₂O@C, Ru_{4.76}/Cu–Cu₂O@C and Ru_{5.59}/Cu–Cu₂O@C (Table S1). The sample with 4.76 wt% exhibited the highest catalytic activity, which was investigated in detail in this work (denoted above as Ru/Cu–Cu₂O@C).

Acknowledgements

This work has been supported by the National Natural Science Foundation of China (no. 21965005), Natural Science Foundation of Guangxi Province (2021GXNSFAA076001), Project of High-Level Talents of Guangxi (F-KA18015), and Guangxi Technology Base and Talent Subject (GUIKEAD18126001, GUIKE AD20297039).

Conflict of Interest

The authors declare no competing financial interest.

Data Availability Statement

Research data are not shared.

Keywords: density functional calculations · electrocatalysis · hydrogen · porous materials · ruthenium

- [1] L. Su, Y. Zhao, Y. Jin, Z. Liu, H. Cui, W. Luo, *Adv. Funct. Mater.* **2022**, *32*, 2113047.
- [2] Y. Xue, L. Shi, X. Liu, J. Fang, X. Wang, B. P. Setzler, W. Zhu, Y. Yan, Z. Zhuang, *Nat. Commun.* **2020**, *11*, 5651–5651.
- [3] a) M. Ma, G. Li, W. Yan, Z. Wu, Z. Zheng, X. Zhang, Q. Wang, G. Du, D. Liu, Z. Xie, Q. Kuang, L. Zheng, *Adv. Energy Mater.* **2022**, *12*, 2103336; b) H. T. Chung, U. Martinez, I. Matanovic, Y. S. Kim, *J. Phys. Chem. Lett.* **2016**, *7*, 4464–4469.
- [4] L. Su, D. Gong, Y. Jin, J. Pei, Y. Liu, J. Li, W. Chen, D. He, D. Wang, Y. Li, *Nano Lett.* **2020**, *20*, 3442–3448.
- [5] T. Tang, L. Ding, Z. C. Yao, H. R. Pan, J. S. Hu, L. J. Wan, *Adv. Funct. Mater.* **2021**, *32*, 2107479.
- [6] L. Su, D. Gong, Y. Jin, D. Wu, W. Luo, *J. Energy Chem.* **2022**, *66*, 107–122.
- [7] a) J. Wang, X. Dong, J. Liu, W. Li, L. T. Rong, J. Xiao, L. Jiang, *ACS Catal.* **2021**, *11*, 7422–7428; b) X. Tian, P. Zhao, W. Sheng, *Adv. Mater.* **2019**, *31*, 1808066.
- [8] Y. Qiu, L. Xin, Y. Li, I. T. McCrum, F. Guo, T. Ma, Y. Ren, Q. Liu, L. Zhou, S. Gu, M. J. Janik, W. Li, *J. Am. Chem. Soc.* **2018**, *140*, 16580–16588.
- [9] Y. Duan, Z.-Y. Yu, L. Yang, L.-R. Zheng, C.-T. Zhang, X.-T. Yang, F.-Y. Gao, X.-L. Zhang, X. Yu, R. Liu, H.-H. Ding, C. Gu, X.-S. Zheng, L. Shi, J. Jiang, J.-F. Zhu, M.-R. Gao, S.-H. Yu, *Nat. Commun.* **2020**, *11*, 4789.
- [10] J. Xu, T. Liu, J. Li, B. Li, Y. Liu, B. Zhang, D. Xiong, I. Amorim, W. Li, L. Liu, *Energy Environ. Sci.* **2018**, *11*, 1819–1827.
- [11] J. Jiang, S. Tao, Q. He, J. Wang, Y. Zhou, Z. Xie, W. Ding, Z. Wei, *J. Mater. Chem. A* **2020**, *8*, 10168–10174.
- [12] Y. Yang, X. Shao, S. Zhou, P. Yan, T. T. Isimjan, X. Yang, *ChemSusChem* **2021**, *14*, 2992–3000.
- [13] F. Zhang, Y. Wei, X. Wu, H. Jiang, W. Wang, H. Li, *J. Am. Chem. Soc.* **2014**, *136*, 13963–13966.

- [14] J. Zhu, F. Chen, Z. Zhang, M. Li, Q. Yang, Y. Yang, Z. Bao, Q. Ren, *ACS Sustainable Chem. Eng.* **2019**, *7*, 12955–12963.
- [15] L. Qin, R. Ru, J. Mao, Q. Meng, Z. Fan, X. Li, G. Zhang, *Appl. Catal. B* **2020**, *269*, 118754.
- [16] Z. Yang, T. Kang, Y. Ji, J. Li, Y. Zhu, H. Liu, X. Jiang, Z. Zhong, F. Su, *J. Colloid Interface Sci.* **2021**, *589*, 198–207.
- [17] X. Luo, Z. Li, M. Luo, C. Guo, L. Sun, S. Lan, R. Luo, L. Huang, Y. Qin, Z. Luo, *J. Mater. Chem. A* **2020**, *8*, 9832–9842.
- [18] Y. Peng, Y. Zhang, A. Guo, M. Mao, Y. Wang, Y. Long, G. Fan, *Chem. Eng. J.* **2021**, *433*, 133648.
- [19] X. Shao, Y. Yang, Y. Liu, P. Yan, S. Zhou, T. Taylor Isimjan, X. Yang, *J. Colloid Interface Sci.* **2022**, *607*, 826–835.
- [20] X. F. Lu, L. Yu, J. Zhang, X. W. Lou, *Adv. Mater.* **2019**, *0*, 1900699.
- [21] R. Zhang, L. Hu, S. Bao, R. Li, L. Gao, R. Li, Q. Chen, *J. Mater. Chem. A* **2016**, *4*, 8412–8420.
- [22] a) H. Xu, X. Niu, Z. Liu, M. Sun, Z. Liu, Z. Tian, X. Wu, B. Huang, Y. Tang, C. H. Yan, *Small* **2021**, *17*, 2103064; b) Y. Yang, Q. Dai, L. Shi, Y. Liu, T. T. Isimjan, X. Yang, *J. Phys. Chem. Lett.* **2022**, *13*, 2107–2116.
- [23] Y. Jiang, M. Yang, M. Qu, Y. Wang, Z. Yang, Q. Feng, X. Deng, W. Shen, M. Li, R. He, *J. Mater. Chem. A* **2020**, *8*, 10409–10418.
- [24] Y. Shi, D. Zhang, H. Miao, X. Wu, Z. Wang, T. Zhan, J. Lai, L. Wang, *Sci. China Chem.* **2022**, *65*, 1829–1837.
- [25] S. Zhou, Y. Yang, W. Zhang, X. Rao, P. Yan, T. T. Isimjan, X. Yang, *J. Colloid Interface Sci.* **2021**, *591*, 221–228.
- [26] C. Li, J. Hou, J. Zhang, X. Li, S. Jiang, G. Zhang, Z. Yao, T. Liu, S. Shen, Z. Liu, X. Xia, J. Xiong, Y. Yang, *Sci. China Chem.* **2022**, *65*, 1420–1432.
- [27] P. Liu, E. J. Hensen, *J. Am. Chem. Soc.* **2013**, *135*, 14032–14035.
- [28] X. Zhou, X. Zhai, G. Ge, J. Dan, K. Pan, J. Tian, R. Sun, B. Dai, H. Pfeiffer, F. Yu, *Chem. Eng. J.* **2020**, *388*, 124270.
- [29] B. Qin, H. Yu, X. Gao, D. Yao, X. Sun, W. Song, B. Yi, Z. Shao, *J. Mater. Chem. A* **2018**, *6*, 20374–20382.
- [30] Y. Yang, Y. Huang, S. Zhou, Y. Liu, L. Shi, T. Taylor Isimjan, X. Yang, *J. Energy Chem.* **2022**, *72*, 395–404.
- [31] L. Li, S. Liu, C. Zhan, Y. Wen, Z. Sun, J. Han, T.-S. Chan, Q. Zhang, Z. Hu, X. Huang, *Energy Environ. Sci.* **2023**, *16*, 157–166.
- [32] a) D. Liu, S. Lu, Y. Xue, Z. Guan, J. Fang, W. Zhu, Z. Zhuang, *Nano Energy* **2019**, *59*, 26–32; b) B. Qin, H. Yu, J. Jia, C. Jun, X. Gao, D. Yao, X. Sun, W. Song, B. Yi, Z. Shao, *Nanoscale* **2018**, *10*, 4872–4881; c) S. St. John, R. W. Atkinson, K. A. Unocic, R. R. Unocic, T. A. Zawodzinski, A. B. Papandrew, *ACS Catal.* **2015**, *5*, 7015–7023; d) J. Wu, Y. Zhou, H. Nie, K. Wei, H. Huang, F. Liao, Y. Liu, M. Shao, Z. Kang, *J. Energy Chem.* **2022**, *66*, 61–67; e) F. Yang, L. Fu, G. Cheng, S. Chen, W. Luo, *J. Mater. Chem. A* **2017**, *5*, 22959–22963.
- [33] Y. Cong, I. T. McCrum, X. Gao, Y. Lv, S. Miao, Z.-G. Shao, B. Yi, H. Yu, M. J. Janik, Y. Song, *J. Mater. Chem. A* **2019**, *7*, 3161–3169.
- [34] X. Ji, Y. Lin, J. Zeng, Z. Ren, Z. Lin, Y. Mu, Y. Qiu, J. Yu, *Nat. Commun.* **2021**, *12*, 1380.
- [35] A. Salah, H.-D. Ren, N. Al-Ansi, F.-Y. Yu, Z.-L. Lang, H. Tan, Y.-G. Li, *J. Mater. Chem. A* **2021**, *9*, 20518–20529.
- [36] a) G. Chen, T. Wang, J. Zhang, P. Liu, H. Sun, X. Zhuang, M. Chen, X. Feng, *Adv. Mater.* **2018**, *30*, 1706279; b) D. Li, X. Chen, Y. Lv, G. Zhang, Y. Huang, W. Liu, Y. Li, R. Chen, C. Nuckolls, H. Ni, *Appl. Catal. B* **2020**, *269*, 118824.
- [37] X. Jiang, H. Jang, S. Liu, Z. Li, M. G. Kim, C. Li, Q. Qin, X. Liu, J. Cho, *Angew. Chem. Int. Ed.* **2021**, *60*, 4110–4116; *Angew. Chem.* **2021**, *133*, 4156–4162.
- [38] a) D. Zhao, Z. Li, X. Yu, W. Zhou, Q. Wu, Y. Luo, N. Wang, A. Liu, L. Li, S. Chen, *Chem. Eng. J.* **2022**, *450*, 138254; b) G. Meng, H. Tian, L. Peng, Z. Ma, Y. Chen, C. Chen, Z. Chang, X. Cui, J. Shi, *Nano Energy* **2021**, *80*, 105531; c) J. Yu, X. Wang, X. Huang, J. Cao, Q. Huo, L. Mi, H. Yang, Q. Hu, C. He, *Chem. Eng. J.* **2022**, *446*, 137248; d) T. Liu, S. Wang, Q. Zhang, L. Chen, W. Hu, C. M. Li, *Chem. Commun.* **2018**, *54*, 3343–3346; e) Q. Song, X. Qiao, L. Liu, Z. Xue, C. Huang, T. Wang, *Chem. Commun.* **2019**, *55*, 965–968; f) D. Luo, B. Zhou, Z. Li, X. Qin, Y. Wen, D. Shi, Q. Lu, M. Yang, H. Zhou, Y. Liu, *J. Mater. Chem. A* **2018**, *6*, 2311–2317; g) B. Lu, L. Guo, F. Wu, Y. Peng, J. E. Lu, T. J. Smart, N. Wang, Y. Z. Finfrock, D. Morris, P. Zhang, N. Li, P. Gao, Y. Ping, S. Chen, *Nat. Commun.* **2019**, *10*, 631; h) Z. Zhang, P. Li, Q. Wang, Q. Feng, Y. Tao, J. Xu, C. Jiang, X. Lu, J. Fan, M. Gu, H. Li, H. Wang, *J. Mater. Chem. A* **2019**, *7*, 2780–2786; i) Q. Hu, G. Li, X. Huang, Z. Wang, H. Yang, Q. Zhang, J. Liu, C. He, *J. Mater. Chem. A* **2019**, *7*, 19531–19538; j) W. Gou, J. Li, W. Gao, Z. Xia, S. Zhang, Y. Ma, *ChemCatChem* **2019**, *11*, 1970–1976; k) D. Zhang, H. Miao, X. Wu, Z. Wang, H. Zhao, Y. Shi, X. Chen, Z. Xiao, J. Lai, L. Wang, *Chin. J. Catal.* **2022**, *43*, 1148–1155.
- [39] X. Zhang, F. Zhou, S. Zhang, Y. Liang, R. Wang, *Adv. Sci.* **2019**, *6*, 1900090.
- [40] Y. Xu, R. Wang, J. Wang, J. Li, T. Jiao, Z. Liu, *Chem. Eng. J.* **2021**, *417*, 129233.
- [41] a) Y. Zhao, X. Wang, G. Cheng, W. Luo, *ACS Catal.* **2020**, *10*, 11751–11757; b) O. H. N. B. Hammer, J. K. Nørskov, *Catal. Lett.* **1997**, *46*, 31–35.
- [42] H. Du, Z. Du, T. Wang, B. Li, S. He, K. Wang, L. Xie, W. Ai, W. Huang, *Adv. Mater.* **2022**, *34*, 2204624.
- [43] Y. Hu, Z. Luo, M. Guo, J. Dong, P. Yan, C. Hu, T. T. Isimjan, X. Yang, *Chem. Eng. J.* **2022**, *435*, 134795.
- [44] F. Yang, X. Bao, P. Li, X. Wang, G. Cheng, S. Chen, W. Luo, *Angew. Chem. Int. Ed.* **2019**, *58*, 14179–14183; *Angew. Chem.* **2019**, *131*, 14317–14321.
- [45] a) M. K. Kundu, T. Bhowmik, R. Mishra, S. Barman, *ChemSusChem* **2018**, *11*, 2388–2401; b) C. Song, Z. Zhao, X. Sun, Y. Zhou, Y. Wang, D. Wang, *Small* **2019**, *15*, 1804268.
- [46] W. Sheng, M. Myint, J. G. Chen, Y. Yan, *Energy Environ. Sci.* **2013**, *6*, 1509–1512.
- [47] M. Fang, Y. Ji, S. Geng, J. Su, Y. Li, Q. Shao, J. Lu, *ACS Appl. Nano Mater.* **2022**, *5*, 17496–17502.
- [48] C. Li, H. Jang, S. G. Liu, M. G. Kim, L. Q. Hou, X. E. Liu, J. Cho, *Adv. Energy Mater.* **2022**, *12*, 2200029.
- [49] Q. T. Feng, T. L. Li, Y. D. Miao, Y. W. Sui, B. Xiao, Z. Sun, J. Q. Qi, F. X. Wei, Q. K. Meng, Y. J. Ren, X. L. Xue, *J. Colloid Interface Sci.* **2022**, *608*, 227–238.

Manuscript received: November 11, 2022
Revised manuscript received: January 26, 2023
Accepted manuscript online: January 26, 2023
Version of record online: March 17, 2023